Chinese Physics Letters

LETTER

Unified Architecture for Continuous-Variable Quantum Cryptography Communication over a Free-Space Channel

Cite as: Tianxiang Zhan *et al*. 2026 *Chin. Phys. Lett.* **43** 090602

DOI CSTR

Recommended Articles

Practical 15 Mb/s Quantum Key Distribution Using Compact Single-Photon Detectors
Tingting Shi, Zhengyu Yan, Yuanbin Fan, Lai Zhou, Yuanfei Gao, Davide G. Marangon, and Zhiliang Yuan
Chin. Phys. Lett. **42**, 120602 (2025)

Anti-Interference High-Speed Modulation Decoder for Quantum Key Distribution
Hua-Xing Xu, Shao-Hua Wang, Chang-Lei Wang, and Ping Zhang
Chin. Phys. Lett. **42**, 010303 (2025)

Parameters Optimization of Decoy-State Phase-Matching Quantum Key Distribution Based on the Nature-Inspired Algorithms
Chang Liu, Yue Li, Haoyang Wang, Kaiyi Shi, Duo Ma, Yujia Zhang, and Haiqiang Ma
Chin. Phys. Lett. **42**, 010301 (2025)

Correlation-Pattern-Based Orbital Angular Momentum Entanglement Measurement Through Neural Networks
Jiaxian Zhao, Zhifeng Liu, Chenghou Tu, Yongnan Li, and Hui-Tian Wang
Chin. Phys. Lett. **42**, 030205 (2025)

A series journal of Chinese Physical Society distributed by IOP Publishing

Chinese Physics Letters

Chin. Phys. Lett. **43** 090602 (2026)

LETTER

DOI: 10.1088/0256-307X/43/9/090602
CSTR: 32039.14.0256-307X.43.9.090602

Unified Architecture for Continuous-Variable Quantum Cryptography Communication over a Free-Space Channel

Tianxiang Zhan(展天翔)[1,2], Peng Huang(黄鹏)[1,2,3,4,*], Huasheng Li(李华生)[5], Piao Tan(谭飘)[1,2], Xu Liu(刘旭)[1,2], Tao Wang(王涛)[1,2,3,4], and Guihua Zeng(曾贵华)[1,2,3,4,5]

[1]State Key Laboratory of Photonics and Communications, School of Automation and Intelligent Sensing, Shanghai Jiao Tong University, Shanghai 200240, China
[2]School of Integrated Circuits (School of Information Science and Electronic Engineering), Shanghai Jiao Tong University, Shanghai 200240, China
[3]Shanghai Research Center for Quantum Sciences, Shanghai 201315, China
[4]Hefei National Laboratory, Hefei 230088, China
[5]Shanghai XunTai Quantech Co., Ltd, Shanghai 200241, China

[*]Corresponding author. Email: huang.peng@sjtu.edu.cn

Quantum cryptography communication encompasses both quantum key distribution (QKD) and the encryption and decryption of plaintext. Continuous-variable QKD (CVQKD) leverages the fundamental principles of physics to enable legitimate parties to share secure keys, while the CVQKD-compatible quantum noise stream cipher (QNSC) exploits quantum fluctuations to further obscure the ciphertext encrypted with these keys. Integrating these two functionalities into a unified system represents a promising developmental trend. However, existing integrated architectures typically rely on multiplexing two separate optical paths and have been demonstrated exclusively over optical fibers. Here, a unified local local oscillator (LLO) quantum cryptography architecture operating over a free-space channel is proposed and experimentally demonstrated. Requiring only simple software-defined switching, our payload-efficient architecture executes both CVQKD and QNSC functionalities utilizing a single optical setup. Over an indoor free-space channel with emulated time-varying atmospheric disturbances, an asymptotic secret key rate of 35.4292 kbps is obtained at a maximum channel attenuation of 19.5054 dB for the CVQKD mode. For the QNSC mode, an encrypted image is successfully transmitted, yielding pixel accuracies of 99.58% and 96.39% under channel attenuations of 10.1690 dB and 12.0620 dB, respectively. This work validates the feasibility of integrated quantum cryptography architectures in complex environments, marking a meaningful step toward constructing payload-constrained quantum communication networks.

Introduction

With the rapid advancement of quantum computing technology, traditional encryption schemes based on computational complexity face severe security vulnerabilities [1]. Quantum communication has garnered widespread attention due to its capability to resist such attacks. Quantum communication encompasses quantum key distribution (QKD) and the encryption and decryption of plaintext using the generated keys. Grounded in the fundamental principles of quantum mechanics, QKD enables communicating parties to share unconditionally secure keys and is typically categorized into discrete-variable (DV) [2] and continuous-variable (CV) [3,4] approaches. CVQKD generally encodes information into the non-commuting quadrature components of optical coherent states. The optical field is modulated using amplitude modulators, phase modulators, or in-phase and quadrature (IQ) modulators, and is subsequently demodulated via the coherent detector. The reliance on these standard telecommunication components affords CVQKD a lower implementation cost compared to DV-QKD and ensures excellent compatibility with existing optical communication networks. Furthermore, the CVQKD scheme employing Gaussian modulation achieves the highest theoretical upper bound [5]. For encryption schemes, the one-time pad [6] strictly requires the key to be as long as the plaintext, which fundamentally restricts the communication speed to the QKD rate. In contrast, quantum noise stream cipher (QNSC), derived from the Y-00 protocol [7, 8], allows for a certain degree of key expansion by leveraging quantum fluctuations to mask adjacent ciphertext states. This physical-layer mechanism exponentially elevates the attack complexity for eavesdroppers, thereby providing a robust, physics-backed safeguard. As two indispensable stages of secure transmission, integrating them into a unified system represents a promising developmental trend for the future of quantum communication.

Integrated quantum secure communication systems incorporating both CVQKD and QNSC functionalities have been previously proposed and experimentally demonstrated [9,10]. However, these integrated architectures inherently rely on the multiplexing of two separate optical paths and are currently confined exclusively to optical fiber channels. To construct large-scale and flexible quantum networks [11], especially in scenarios where deploying optical fibers is physically or economically impractical—such as satellite-to-ground links [12−15], mountain peaks [16], sea surfaces [17], or mobile platforms like drones [18]—free-space atmospheric channels are indispensable. While the individual implementations of CVQKD [19−23] and QNSC [24,25] over atmospheric or free-space channels have been successfully demonstrated, their integration within a unified free-space architecture remains unexplored—particularly under dynamic, turbulent conditions where QNSC performance has not yet been experimentally verified.

In this Letter, we propose and experimentally demonstrate a local local oscillator (LLO) quantum cryptography communication system operating over a free-space channel. Distinct from previous approaches that integrate two separate optical paths [9,10], our scheme employs a unified optical setup to realize both CVQKD and QNSC functionalities through software-defined switching. This architecture effectively reduces implementation costs and is highly adaptable to practical free-space scenarios with stringent payload constraints, such as drones and satellites. To address channel-induced impairments, digital signal processing algorithms [22,26,27] are utilized to correct the time-varying frequency offset between the transmitter and receiver lasers, as well as to compensate for the phase drift between the

Received 18 June 2026; accepted 21 August 2026; published 17 September 2026
© 2026 Chinese Physical Society and IOP Publishing Ltd. All rights, including for text and data mining, AI training, and similar technologies, are reserved.

Check for updates

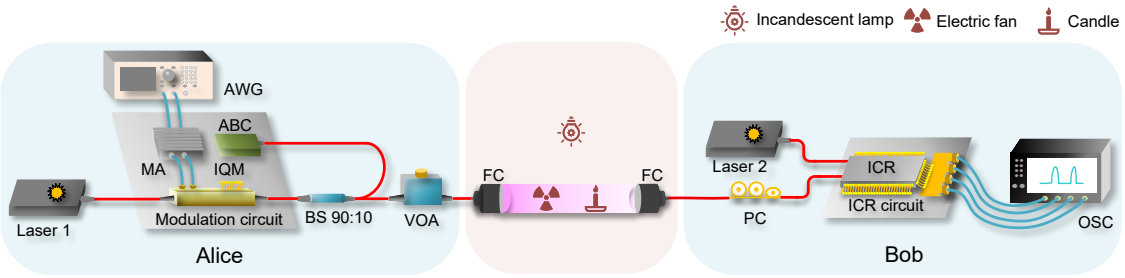

Fig. 1. Optical layout of the CV quantum cryptography communication system. Red lines represent optical signal paths, while cyan lines represent electrical signal paths. The icons of an incandescent lamp, an electric fan, and a candle indicate that the corresponding items are placed within the channel to simulate background sunlight and thermal turbulence. AWG, arbitrary waveform generator; ABC, automatic bias controller; MA, microwave amplifier; IQM, in-phase and quadrature modulator; BS, beam splitter; VOA, variable optical attenuator; FC, fiber collimator; PC, polarization controller; ICR, integrated coherent receiver; OSC, oscilloscope.

signal and the local oscillator (LO). Furthermore, a pilot tone is employed to dynamically estimate the fluctuating channel transmittance. For CVQKD, we achieve a secret key rate of 35.4292 kbps in the asymptotic regime, operating under a channel attenuation of 19.5054 dB accompanied by artificial thermal turbulence and incandescent illumination. For QNSC, we performed an image transmission at a symbol rate of 500 MBaud via a phase-encoding scheme, yielding pixel accuracy rates of 99.58% and 96.39% under channel attenuations of 10.1690 dB and 12.0620 dB, respectively. This work not only presents the first experimental implementation of QNSC over a dynamic, turbulent free-space channel, but also validates the feasibility of integrating CVQKD and QNSC within a unified architecture in complex atmospheric environments, and represents a meaningful step toward the future construction of quantum secure communication networks.

Theoretical Scheme

In our software-defined architecture, the secure key generation is governed by the CVQKD protocol based on Gaussian-modulated coherent states. During this operation mode, Alice generates two independent and identically distributed sequences of real-valued Gaussian random numbers, $\{x_A\}$ and $\{p_A\}$, with zero mean and variance V_A, and utilizes them to modulate the optical field, thereby preparing a sequence of coherent states $\{|x_A + \mathrm{i}p_A\rangle\}$. Alice transmits these states to Bob through the channel, where Bob performs heterodyne detection on the received states [28]. Subsequently, Alice and Bob apply reverse reconciliation to obtain a common raw key, which is then distilled into the final secret key via reconciliation and privacy amplification. The asymptotic secret key rate with the Devetak–Winter bound [29] is given by [30]

$$R = f(1-\alpha)(1-\upsilon)(1-\mathrm{FER})(\beta I_{AB} - \chi_{BE}), \tag{1}$$

where I_{AB} represents the classical mutual information between Alice and Bob, and χ_{BE} denotes the Holevo bound on the information leaked to Eve [see Supplemental Material (SM) for more details]. Additionally, f is the symbol rate of the quantum signal, α is the overhead for frame synchronization, υ is the fraction of data revealed for parameter estimation, FER is the frame error rate, and β is the reconciliation efficiency.

We implement the QNSC protocol employing a phase-encoding scheme. The procedure is detailed as follows:

- Alice utilizes a hash algorithm to expand the secret key generated via CVQKD into a session key.
- Alice extracts l bits from the session key and converts them into a decimal integer. This integer is then reduced modulo M to obtain the encryption key K', where $2M$ denotes the number of equally divided sectors in the phase space, and M is chosen as an odd integer, which ensures that adjacent phase states represent alternating plaintext bits.
- A phase shift operator $\mathscr{U}(\phi_c)$ is applied to the initial coherent state to generate the ciphertext state, given by $|\alpha_c\rangle = \mathscr{U}(\phi_c)|\alpha_0\rangle$. The modulation phase ϕ_c is jointly determined by the plaintext bit s and the encryption key K' as follows:

$$\phi_c = K'\frac{\pi}{M} - \pi(1 \oplus s \oplus (K' \bmod 2)). \tag{2}$$

- Alice transmits the ciphertext to Bob over the channel. At the receiver, Bob applies a local phase shift operator $\mathscr{U}(\phi_d)$ to the received optical signal to obtain the decrypted state $|\alpha_d\rangle = \mathscr{U}(\phi_d)|\alpha_c\rangle$. The decryption phase ϕ_d is exclusively determined by the shared encryption key K':

$$\phi_d = -K'\frac{\pi}{M} + \pi(K' \bmod 2). \tag{3}$$

- Based on the measurement outcomes, Bob determines the plaintext bit. If the measured state is closer to $|\alpha_0 \mathrm{e}^{-j\pi}\rangle$, he determines the plaintext bit to be 0; conversely, if the measured state is closer to $|\alpha_0\rangle$, he determines the plaintext bit to be 1. The inner product between these two states is $\langle\alpha_0 \mathrm{e}^{-j\pi}|\alpha_0\rangle = \mathrm{e}^{-2|\alpha_0|^2}$. When $|\alpha_0| \gg 1$, the inner product approaches zero, allowing the states to be treated as quasi-orthogonal and facilitating plaintext recovery via binary decision.

To address the relative frequency offset in the LLO scheme, a pilot-assisted compensation method is deployed. Accounting for the signal's carrier frequency f_s, the complex heterodyne measurement outcome is expressed as $\hat{y}_{het} = (\hat{x} + \mathrm{i}\hat{p})\mathrm{e}^{-\mathrm{i}\{2\pi[\Delta f(t)+f_s]t-\Delta\theta_0(t)\}}$, where $\Delta f(t)$ is the frequency offset between the two independent lasers and $\Delta\theta_0(t)$ is the initial phase difference. Concurrently, a high-energy pilot tone centered at a carrier frequency f_p is co-transmitted via frequency-division multiplexing, yielding the measurement outcome $A\mathrm{e}^{-\mathrm{i}\{2\pi[\Delta f(t)+f_p]t-\Delta\theta_0(t)\}}$. Since the pilot tone and the signal undergo identical transmission and detection processes, the phase compensation factor C_{comp} derived from the pilot tone is given by

$$C_{comp} = \mathrm{e}^{\mathrm{i}\{2\pi[\Delta f(t)+f_p]t-\Delta\theta_0(t)\}}. \tag{4}$$

Finally, multiplying $\hat{y}_{het}$ by C_{comp} followed by a digital phase rotation of $\mathrm{e}^{\mathrm{i}2\pi(f_p-f_s)t}$ completely cancels out the time-varying noise terms, successfully recovering the states $\hat{x} + \mathrm{i}\hat{p}$ (see SM for more details).

Experimental Setup

Both the CVQKD and QNSC protocols share the exact same hardware configuration, requiring only a software-level toggle to switch between the two modes. The schematic of the experimental setup is depicted in Fig. 1. Both protocols are implemented using a LLO scheme. To compensate for the relative frequency offset between the two independent lasers, a pilot tone is co-transmitted with the signal. The upsampled signals undergo pulse shaping via a root-raised-cosine (RRC) filter with a 0.2 roll-off factor, followed by carrier modulation. The pilot tone, bypassing the RRC filtering, is frequency-division multiplexed with the signals. A narrow-linewidth laser (Laser 1) emits a continuous-wave beam centered at 1550.1202 nm. This optical field is then fed into an IQM, which modulates both the signal and

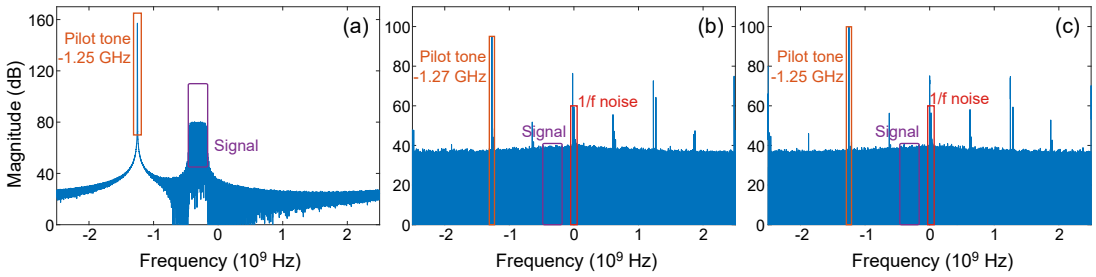

Fig. 2. Spectral evolution of the signal and the pilot tone in the LLO system. (a) Complex frequency spectrum of the transmitted signal generated by Alice. (b) Complex frequency spectrum of the raw signal detected by Bob. (c) Complex frequency spectrum of the received signal after frequency offset recovery.

Table 1. Signal parameters for the CVQKD and QNSC schemes. Only the distinct parameters are listed.

Parameter	Protocol	
	CVQKD	QNSC
Symbol rate (MBd)	250	500
Upsampling factor	20	10
Spectral bandwidth (MHz)	300	600
Carrier frequency (MHz)	−312.5	−625
Frame length (symbols)	250000	500000
Pilot-to-signal amplitude ratio	16	4

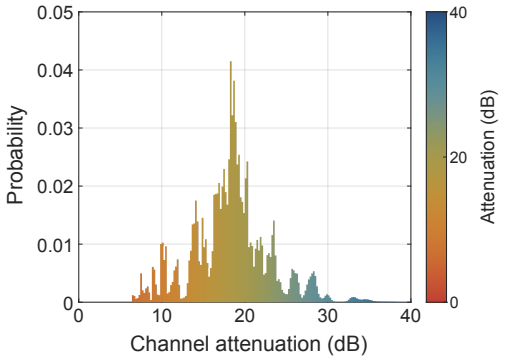

Fig. 3. Probability distribution of the channel attenuation over an 80 cm indoor free-space channel with emulated time-varying atmospheric disturbances.

the pilot tone onto it. The electrical driving signals for the IQM are generated by a 16-bit arbitrary waveform generator (AWG) operating at a sampling rate of 5 GS/s. A closed-loop feedback mechanism for the IQM is established using an external 90:10 beam splitter (BS) and the controller's built-in photodiode. Specifically, 10% of the split optical power is fed back to the automatic bias controller (ABC) to regulate the bias point of the IQM, while the remaining 90% is directed into the variable optical attenuator (VOA) for attenuation.

After being attenuated to an appropriate power by the VOA, the modulated optical field is emitted into a free-space channel via a fiber collimator (FC). Constrained by the physical dimensions of the optical breadboard, our free-space optical path spans approximately 80 cm. To emulate a long-distance transmission scenario over this short distance, we intentionally introduced a spatial misalignment between the transmitting and receiving FCs, yielding a channel attenuation of about 20 dB. Furthermore, to mimic real-world atmospheric conditions, an electric fan and a burning candle were placed along the optical path to generate wind-induced and thermal turbulence, while an incandescent lamp was positioned approximately 50 cm above the channel to simulate background sunlight interference.

Upon reception by the FC at Bob's side, the optical field first undergoes polarization alignment via a polarization controller (PC). To achieve more precise polarization adjustment, we utilize one channel of the oscilloscope to monitor the orthogonal polarization component separated by the polarization beam splitter (PBS) built into the integrated coherent receiver (ICR). Laser 2 generates the LO beam with a central wavelength of 1550.1214 nm and an optical power of approximately 12 dBm, which is then directed into the ICR alongside the signal and pilot tone for heterodyne detection. The oscilloscope and the AWG are clock-synchronized by sharing a clock reference signal via an radio-frequency cable.

In the digital signal processing routine, the pilot tone is digitally generated with a fixed carrier frequency of −1.25 GHz to facilitate frequency-division multiplexing. However, the CVQKD and QNSC protocols adopt different signal carrier frequencies. All the differing parameters between the two protocols are summarized in Table 1. Despite these parameter variations, both protocols share an identical digital signal processing pipeline, employing the exact same algorithm to compensate for the relative phase drift induced by the frequency offset between the two lasers. Without loss of generality, we use the CVQKD protocol as an example to illustrate this compensation method. Figure 2(a) illustrates the complex spectrum of the signal transmitted by Alice, where the quantum signal is centered at −312.5 MHz with a spectral width of 300 MHz. Figure 2(b) depicts the complex spectrum of the signal received by Bob. During the experiment, the relative wavelengths of the two lasers were finely tuned to minimize the beat noise peaks in the spectrum. However, due to the residual frequency offset between the two lasers, the received signal and pilot tone experience a common phase drift. As a result, the center frequency of the pilot tone shifts to approximately −1.27 GHz. By comparing this shifted pilot tone with the originally transmitted reference, the exact location of the quantum signal can be accurately deduced. Specifically, the compensation factor C_{comp} can be calculated from the pure pilot tone extracted by filtering out the signal. By applying C_{comp}, a global relative phase compensation is performed on both the received signal and the pilot tone to eliminate the noise induced by the frequency offset between the two lasers. The compensated spectrum is presented in Fig. 2(c), where the center frequency of the pilot tone returns to −1.25 GHz, and the quantum signal is restored to its original transmission frequency band. Subsequently, we down-convert the quantum signal to the baseband and apply an appropriate low-pass filter to completely remove the pilot tone.

By publicly disclosing a subset of their data, Alice and Bob achieve frame synchronization and extract data sequences of identical length. Subsequently, Bob applies a matched RRC filter—identical to the one used by Alice—to the received data to recover the Gaussian symbols. Based on the partially disclosed data from Alice, Bob performs a fine phase compensation on the recovered Gaussian symbols by sweeping the phase rotation across 360° to minimize the phase excess noise. To mitigate the leakage induced by IQ modulator imperfections, Bob compensates for this effect by calculating the leakage coefficient through the cross-correlation between the I and Q channels. Please see SM for a summary of the system architecture.

Prior to initiating the formal quantum communication, a back-to-back calibration of the pilot tone is performed on the experimental setup. Specifically, the transmitter and receiver are connected using an ultra-short optical fiber with negligible attenuation. The received

Table 2. Experimental parameters and results of the CVQKD protocol over the indoor free-space channel with emulated time-varying atmospheric disturbances. L, average channel attenuation; V_A, modulation variance; ν_{el}, electronic noise; SNR, signal-to-noise ratio; ε, excess noise; R, secret key rate.

	L (dB)	V_A	ν_{el}	SNR	ε	R (kbps)
i	11.5270	5.9217	0.1376	0.1373	0.0096	431.9192
ii	13.1526	6.3685	0.1364	0.1016	0.0358	190.3495
iii	14.1493	6.3377	0.1358	0.0804	0.0394	136.1973
iv	15.1747	6.3282	0.1360	0.0634	0.0284	127.9751
v	19.5054	6.5717	0.1365	0.0243	0.0357	35.4292

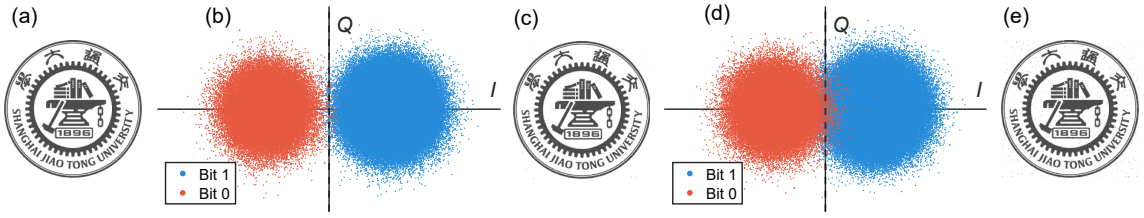

Fig. 4. Experimental results of the encrypted image transmission over the indoor free-space channel with emulated time-varying atmospheric disturbances. (a) The original binary bitmap of the Shanghai Jiao Tong University logo. (b) The decrypted constellation diagram and (c) the corresponding recovered image under a channel attenuation of 10.1690 dB, with a pixel accuracy of 99.58%. (d) The decrypted constellation diagram and (e) the corresponding recovered image under a channel attenuation of 12.0620 dB, with a pixel accuracy of 96.39%. The received data points in the constellations are color-coded based on their true transmitted bits (blue for bit 1, red for bit 0).

pilot tone power is measured and recorded as the zero-loss reference value. During the experiment, the real-time channel attenuation is derived from the comparison between the instantaneous pilot power and this pre-calibrated reference. This calibration method is applicable to both the CVQKD and QNSC protocols. We continuously monitored the characteristics of the indoor free-space channel with emulated dynamic atmospheric disturbances for one hour, obtaining the probability distribution of the channel attenuation as depicted in Fig. 3. Here, the statistical bin width is set to 0.2 dB, and the channel attenuation is primarily distributed between 5 dB and 40 dB. Notably, at certain instances, the channel attenuation falls below the 20 dB of the turbulence-free scenario. This occurs because the turbulence-induced beam wander occasionally compensates for the intentional spatial misalignment of FC.

Experimental Results

We conducted quantum cryptographic experiments, encompassing both the CVQKD and QNSC protocols, over the indoor free-space channel with emulated time-varying atmospheric disturbances. The inherent mode selectivity of coherent detection [31] enables our system to operate resiliently under background incandescent and candle light without an additional narrow-band spectral filter. For CVQKD, we estimated key parameters including the excess noise, electronic noise, modulation variance, and channel attenuation, and subsequently evaluated the secret key rate, as summarized in Table 2. The values of α and υ are 1% and 10%, respectively, while the quantum efficiency of the detector is 37.5%. The frame length is set to 2.5×10^5 symbols, corresponding to a brief acquisition duration of only 1 ms, ensuring that the channel attenuation remains relatively stable within a single frame. In our current experimental demonstration, the post-processing steps of reconciliation and privacy amplification were not implemented; consequently, the reported secret key rate represents an estimated value. However, drawing upon our previous CVQKD field trial [23] over a practical atmospheric channel—which incorporated complete post-processing—we set the FER and β to 96.5% and 80%, respectively. Ultimately, under the asymptotic assumption, we achieved a secret key rate of 35.4292 kbps at a maximum channel attenuation of 19.5054 dB, with an estimated excess noise of 0.0357 SNU.

Employing the QNSC protocol with M set to 1023, we utilized the keys to transmit a black-and-white image of the Shanghai Jiao Tong University logo (where each pixel is represented by an 8-bit binary sequence), as shown in Fig. 4(a). As the legitimate party possessing the secret key, Bob can successfully decrypt the ciphertext—encrypted by Alice using Eq. (2)—back into plaintext via Eq. (3). Under a channel attenuation of 10.1690 dB, the decrypted constellation diagram and the recovered image are shown in Figs. 4(b) and 4(c), respectively. To intuitively visualize the bit errors, the received data points are color-coded based on their true transmitted bit values. Under the influence of channel noise, the data points, which should ideally reside at two discrete positions on the positive and negative semi-axes representing bits 1 and 0, broaden into cloud-like clusters. Consequently, points crossing the vertical decision boundary clearly indicate the transmission errors induced by channel noise. At this specific channel attenuation, the constellation diagram reveals that the two signal clusters are nearly tangent to each other, marking the initial emergence of error points. For comparison, the experimental results under a channel attenuation of 12.0620 dB are depicted in Figs. 4(d) and 4(e), where the two signal clusters in the constellation diagram partially overlap, reducing the pixel accuracy to 96.39%.

Conclusion and discussion

In summary, we have proposed and experimentally validated a unified LLO quantum cryptography communication system operating over a free-space channel. By utilizing software-defined switching, the architecture efficiently toggles between secure key generation (CVQKD) and high-speed encrypted data transmission (QNSC) without requiring redundant optical paths. Our experimental setup rigorously emulated practical atmospheric challenges, including dynamic channel attenuation, thermal turbulence, and background light interference. For the CVQKD mode, the system obtained an asymptotic secret key rate of 35.4292 kbps at the maximum channel attenuation of 19.5054 dB. We evaluated the CVQKD performance exclusively in the asymptotic regime because the fluctuating attenuation distributes the received frames across numerous distinct attenuation bins. This fragmentation significantly limits the block size of each data subset, making it highly time-consuming to accumulate a sufficiently large data block within a single bin to rigorously address finite-size effects. For the QNSC mode, the phase-encoding scheme proved highly robust against drastic transmittance variations, successfully transmitting

the encrypted Shanghai Jiao Tong University logo under a channel attenuation of no less than 10 dB. Notably, this also constitutes the first experimental implementation of QNSC over a dynamic, turbulent free-space channel.

Constructed with standard components widely adopted in classical coherent optical systems, the system naturally interfaces seamlessly with existing telecommunication infrastructures. Moving forward, transitioning this integrated architecture from indoor emulations to long-distance outdoor field trials will further verify its potential. Ultimately, this payload-efficient and unified architecture provides a highly promising pathway for establishing future quantum secure communication networks involving satellites, drones, and other mobile platforms.

Acknowledgements

This work was supported by the National Natural Science Foundation of China (Grant No. 62671369), the Quantum Science and Technology-National Science and Technology Major Project (Grant No. 2021ZD0300703), the Shanghai Municipal Science and Technology Major Project (Grant No. 2019SHZDZX01), and the National Key Laboratory of Space Security (Grant No. ZN08-04-2503).

References

[1] Shor P W 1994 *Proceedings 35th Annual Symposium on Foundations of Computer Science* p. 124
[2] Bennett C H and Brassard G 1984 *Proceedings of the International Conference on Computers, Systems and Signal Processing* p. 175
[3] Grosshans F and Grangier P 2002 *Phys. Rev. Lett.* **88** 057902
[4] Zhang Y, Bian Y, Li Z, Yu S, and Guo H 2024 *Appl. Phys. Rev.* **11** 011318
[5] Pirandola S, Laurenza R, Ottaviani C, and Banchi L 2017 *Nat. Commun.* **8** 15043
[6] Vernam G S 1926 *J. AIEE* **45** 109
[7] Yuen H P 2000 *Quantum Communication, Computing, and Measurement 3* (Springer, Boston, MA) p. 285
[8] Yuen H P 2003 arXiv: quant-ph/0311061
[9] Dai W, Lu Y, Zhu J, and Zeng G 2011 *Sci. China Inf. Sci.* **54** 2578
[10] Liu Y, Wang T, Huang P, and Zeng G 2026 *Opt. Lett.* **51** 760
[11] Bian Y, Zhang Y, Yu S, Li Z, and Guo H 2026 *Phys. Rev. Lett.* **136** 080801
[12] Liao S K, Cai W Q, Liu W Y *et al*. 2017 *Nature* **549** 43
[13] Liao S K, Lin J, Ren J G *et al*. 2017 *Chin. Phys. Lett.* **34** 090302
[14] Liao S K, Cai W Q, Handsteiner J *et al*. 2018 *Phys. Rev. Lett.* **120** 030501
[15] Li Y, Cai W Q, Ren J G *et al*. 2025 *Nature* **640** 47
[16] Kurtsiefer C, Zarda P, Halder M, Weinfurter H, Gorman P, Tapster P, and Rarity J 2002 *Nature* **419** 450
[17] Fürst M, Weier H, Schmitt-Manderbach T *et al*. 2006 *Advanced Free-Space Optical Communication Techniques/Applications II and Photonic Components/Architectures for Microwave Systems and Displays* **6399** 124
[18] Tian X H, Yang R, Liu H Y *et al*. 2024 *Phys. Rev. Lett.* **133** 200801
[19] Shen S Y, Dai M W, Zheng X T, Sun Q Y, Zhu B, Guo G C, and Han Z F 2019 *Phys. Rev. A* **100** 012325
[20] Zheng X T, Zhang Q F, Ling J, Guo G C, and Han Z F 2025 *npj Quantum Inf.* **11** 52
[21] Yin H, Huang P, Zhou Z, Wang T, Jiang X, and Zeng G 2025 *npj Quantum Inf.* **11** 134
[22] Liao X, Xu Y, Zhang Q, Huang P, Wang T, Wang K, and Zeng G 2025 *Photonics Res.* **13** 2603
[23] Zhan T, Li H, Huang P *et al*. 2026 *Phys. Rev. Lett.* **136** 100801
[24] Futami F and Hirota O 2014 *Photonics Applications for Aviation, Aerospace, Commercial, and Harsh Environments V* **9202** 216
[25] Futami F and Tanizawa K 2023 *IET Conference Proceedings CP839* **2023** 507
[26] Xu Y, Wang T, Liao X, Zhou Y, Huang P, and Zeng G 2024 *Photonics Res.* **12** 2549
[27] Wu M, Pan Y, Li J *et al*. 2026 *Phys. Rev. X* **16** 021039
[28] Weedbrook C, Lance A M, Bowen W P, Symul T, Ralph T C, and Lam P K 2004 *Phys. Rev. Lett.* **93** 170504
[29] Devetak I and Winter A 2005 *Proc. R. Soc. A* **461** 207
[30] Wang T, Huang P, Li L, Zhou Y, and Zeng G 2024 *New J. Phys.* **26** 023002
[31] Wang S, Huang P, Wang T, and Zeng G 2019 *Phys. Rev. Appl.* **12** 024041